ORIGINAL PAPER

Data analysis and dynamic characteristic investigation of large-scale civil structures monitored by RTK-GNSS based on a hybrid filtering algorithm

Chunbao Xiong[1] · Meng Wang[1] · Wen Chen[1,2]

Abstract

Internal and external factors impacted the safety of large-scale civil engineering structures after their construction. Thus, this study used the real-time kinematic global navigation satellite system (RTK-GNSS) technology to monitor a super-high-rise building and a long-span bridge in China. First, the effects of positioning errors and noise in the different environments were investigated. And this study revealed that the multipath-dominated background noise generated by water is not negligible. To suppress noise, the researchers next proposed a hybrid noise reduction algorithm that combined wavelet threshold (WT) and complete empirical mode decomposition with adaptive noise (CEEMDAN) based on autocorrelation function and cross-correlation coefficient. The results proved that the method applied can weaken noise and maintain adequate information. The noise reduction is the best compared with ensemble empirical mode decomposition (EEMD), CEEMDAN, and EEMD-Chebyshev. Finally, the direction of the main motion of the super-high-rise building is calculated. And the error between the first-order frequency and finite-element analysis is 0.189%, the maximum relative error for the third-order frequency is only 4.379%. The frequencies, damping ratios, and failure probabilities of the Fumin bridge are also obtained under different traffic loads. Furthermore, the intrinsic frequency inaccuracy measured by RTK-GNSS is less than that by the accelerometer in the same monitoring period.

Keywords RTK-GNSS · Dynamic monitoring · Large-scale civil engineering structures · Noise reduction · Hybrid filtering · Characteristic analysis

1 Introduction

Strong wind, temperature, and traffic stress significantly influence large-scale civil infrastructures as time passes, resulting in their deformation or collapse. For instance, the Humen bridge in Guangzhou experienced severe shaking in May 2020. On May 18, 2021, the Shenzhen SEG Plaza building, with a height of 355.8 m, shook violently, endangering the lives of residents. It is essential to implement regular dynamic deformation monitoring to assess the structural properties.

As engineering sophistication advances, a variety of measurement techniques have become ubiquitous in deformation monitoring, such as accelerometers [1, 2], 3D laser scanners [3–5], radar interference systems [6, 7], camera techniques [8, 9], and global navigation satellite systems (GNSS) [10, 11]. Accelerometers, however, suffer from drift during subsequent data integration. Three-dimensional laser scanners can capture the image information of the object, whereas they have relatively high requirements for the operating environment. Radar interference monitoring has high efficiency, yet atmospheric conditions limit the measurement precision, and it only gains one-dimensional projection information. Photogrammetry obtains dynamic responses by taking pictures and video recording. But the hardware level and light intensity affect the imaging quality.

✉ Meng Wang
engwang@tju.edu.cn

Chunbao Xiong
xcb1710737997@163.com

Wen Chen
wm1710737997@163.com

1   School of Civil Engineering, Tianjin University, Tianjin 300350, China

2   College of Science and Technology, Agriculture University of Hebei, Baoding 071001, China

GNSS can get the three-dimensional coordinates of structures by receiving and transmitting specific satellite signals. It has high efficiency, operates easily, and performs continuous real-time monitoring [12–14]. Beshr et al. adopted artificial neural networks (ANNs) and adaptive neuro-fuzzy inference systems (ANFIS) to provide the deformation characteristics of a suspension bridge under GNSS monitoring and to predict the displacement [15]. Zhang et al. used GNSS with an accelerometer to acquire real-time dynamic information about the Jiangyin bridge span. They analyzed the spectral characteristics of the bridge based on a data fusion method [16]. Li et al. monitored the deformation of the super-high-rise building and used an improved fuzzy function method to increase the accuracy of the GPS/BDS [17]. GNSS is sensitive to low-frequency responses and popular in deformation monitoring of large civil projects [18–20].

The instrument itself and the environment introduce several flaws into the GNSS results, including troposphere delay, ionosphere delay, troposphere error, satellite clock difference, and multipath effects. Differential techniques can eliminate the first four errors but not the background noise dominated by multipath [21–23]. At the current stage, filtering is a known active technique to weaken the noise, mainly comprising Chebyshev filtering [24], wavelet transforms [25], and empirical mode decomposition (EMD) [26, 27]. However, Chebyshev filtering requires more covariates, and different input parameters affect noise reduction. In the case of complex signals, a single wavelet transform is not significant for the denoise effect. EMD has adaptivity but generates modal aliasing during decomposition. For the shortcomings of EMD, Wu and Huang proposed EEMD [28], whereas it produced large-signal recombination errors. Yeh improved EEMD by adding positive and negative paired white noise [29], namely, complete ensemble empirical mode decomposition (CEEMD). Nonetheless, its essence is similar to EEMD, where different modes are reserved owing to positive and negative noise. Also, some studies usually choose one screening criterion without solving the problem of correct selection for the intrinsic mode function (IMF) decomposed by EMD or EEMD, or CEEMD [24].

For solving these limitations yet retaining valid information, this paper puts forward CEEMDAN [30–32] based on an autocorrelation function and cross-correlation coefficient. Meanwhile, considering that the single filter method is not apparent in denoising, CEEMDAN is combined with wavelet threshold (WT) to enhance the noise reduction effect.

The modal parameter is a fundamental index for analyzing dynamic properties and is one of the criteria for evaluating structural health, where frequencies and damping play crucial roles [33, 34]. Reasonable discrimination of parameter values naturally excites the interest of engineers. The effectiveness of numerous methods has been verified in experiments such as the peak picking method (PP) [35], stochastic subspace identification (SSI) [36], natural excitation technique (NExT) [37], eigensystem realization algorithm (ERA) [37], random decrement technology (RDT) [38], and Ibrahim time-domain (ITD) [39]. For intricate structural systems, integration of approaches is needed to improve the quality of the parameter identification. This study will exhaustively provide the dynamic characteristics of a long-span bridge based on RDT-ITD.

This paper develops a CEEMDAN-WT filter to reduce the noise in the data of two large-scale civil engineering structures monitored by real-time kinematic-GNSS (RTK-GNSS). And a technique combining the autocorrelation normalization function and cross-correlation coefficient screens the useful IMFs. In the second section, the noise error impact brought by different environments is analyzed. The third section is the methodology and the experimental processing flow. In the fourth section, the RTK-GNSS technology is adopted to monitor the super-high-rise building; then, the noise is reduced by the hybrid filter and modal frequencies are identified. And the RTK-GNSS and accelerometers are simultaneously used to monitor the deformation of a large-span bridge to get parameter information and compare the variations of modal parameters caused by different traffic loads. To the end, a finite-element model (FEM) is established to judge the magnitude of the frequency errors obtained by two sensors, and the safety capability of the bridge is measured. The findings are summarized in the final section.

2 RTK-GNSS positioning errors and noise analysis

In the following parts, both targets were monitored in an environment with a large water-covered area; even though measurement points were at a specified distance from the water, they still could not avoid adverse effects to the results. Simultaneously, it is known from multipath principles that the error size is related to the reflection coefficient of the environment around the receiver antenna. The reflection coefficient varied because of the difference in reflection source media. For those reasons, this paper elected the water area for a test, while the cement floor was compared to explore noise effects.

The test lasted for 8 h was conducted on November 6, 2019, and the radius of the two environments (open cement floor and water) was about 100 m, 50 m. The equipment consisted of three RTK-GNSS receivers, two of which as mobile stations with a sampling frequency of 10 Hz, and the remaining one was the reference station (Fig. 1). The reference station was 600 m and 760 m from the two sites. Because the mobile station location was fixed on the static

Fig. 1 Instrument arrangement: **a** on the cement floor; **b** on the water surface; **c** the reference station
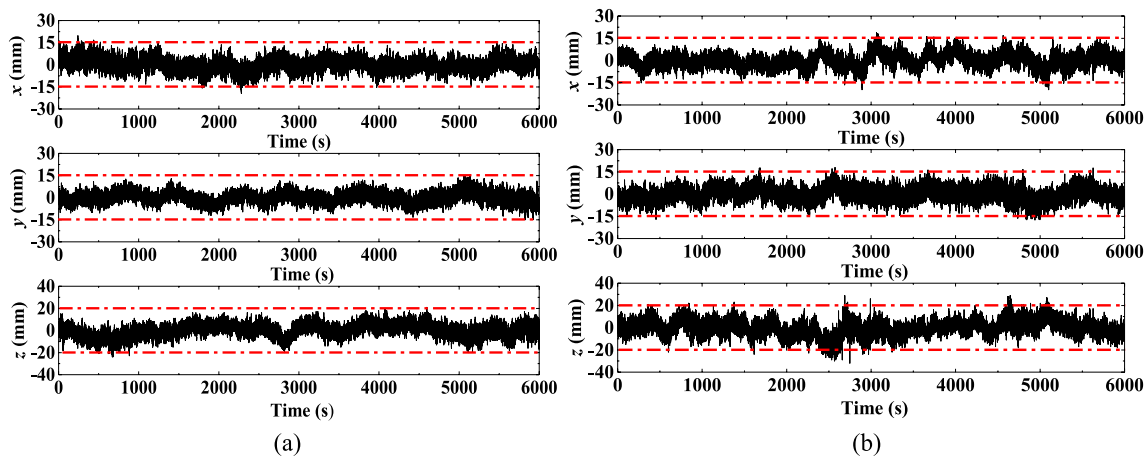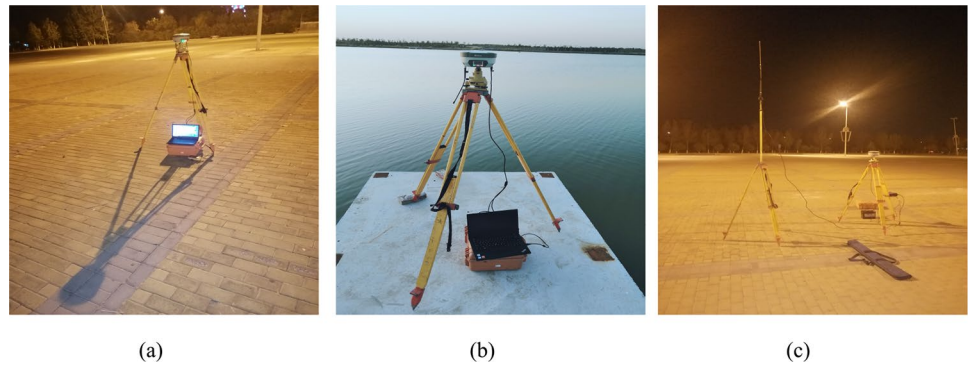
(a) (b) (c)

(a) (b)

Fig. 2 Monitor results of two environments: **a** amplitude for the cement floor; **b** amplitude for the water-covered area

Table 1 Root mean square (RMS) values of amplitude variation (unit: mm)

| Directions	Cement floor	Water
x	4.351	4.598
y	3.572	4.446
z	4.791	7.097

ground and the measurement baseline was short, the coordinates of the positioning points should all be the same in theory. Although there are some errors (such as satellite and ephemeris errors), they can be effectively eliminated by the internal differential of the RTK. However, the coordinates in Fig. 2 change with time; it is known from RTK-GNSS principles and error sources that error is mainly background noise dominated by multipath. It can be seen from Fig. 2 that the two site amplitudes fluctuate within 15 mm in the xy direction. In the z-direction, the amplitude variation is slightly higher, approximately 20 mm.

The root mean square (RMS) values of amplitude variation for the two environments are calculated separately: the smaller the RMS, the smaller the error. In Table 1, the RMS

values of the cement floor are lower than that of water, indicating that the multipath-dominated noise generated by the reflection from the water surface is more serious. In addition, the RMS values in the z-direction are greater than those in the x and y direction for both environments. On one hand, it verifies that the planar positioning precision of RTK-GNSS is better than elevation. On the other hand, it also proves that the accuracy remains around 20 mm under the strong interference of smooth water surface on the RTK received signal, which means the instrument has acceptable stability.

A point cloud map (Fig. 3), drawn from horizontal monitoring data, presents a comprehensive view of the positioning errors in the two environments. After RTK differential processing and error analysis, the difference of the multipath-dominated noise leads to the variation of two points cloud maps. The amplitude variations in the x-direction of the two sites are remarkably similar. In contrast, the y amplitude fluctuation of the water is slightly larger than that of the cement floor. The data dispersion in Fig. 3b is also greater, implying that it may generate bigger errors and should not be ignored. In addition, the shapes of the two-point cloud maps are different: the geometry of the water error cloud is nearly circular, and that of the cement floor is elliptical. This

Fig. 3 Error point cloud diagram for two environments: **a** cement floor; **b** water

(a)

(b)
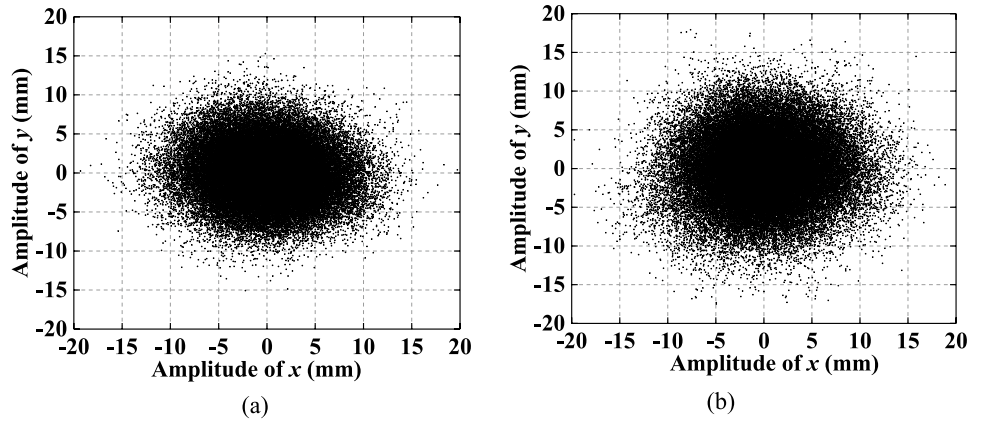
reveals differences in the positions and directions of the two reflection points.

The analysis above helps to understand the background noise distinctions from multiple perspectives. Since the experimental subjects are in a water environment, weakening the monitoring noise errors are necessary.

3 Methodology

3.1 CEEMDAN

CEEMDAN [40] is an improved algorithm based on EMD [41] and EEMD [42]. Its core adds white noise to the original signal at a specific stage in EMD performing. The added white noise can be offset during EMD operation so that the IMFs are decomposed more thoroughly. The steps are as follows:

$$X(t) = x(t) + \varepsilon_0 \omega^i(t), \tag{1}$$
1.

where $x(t)$ is the original signal, $\omega^i(t)$ ($i = 1, 2, \dots, N$) is white noise, and $X(t)$ is the signal after adding white noise.

2. EMD is performed on the signal $X(t)$ to gain $f_1^i(t)$, then the average value is summed and calculated as the first IMF component:

$$\overline{f_1}(t) = \frac{1}{N} \sum_{i=1}^{N} f_1^i(t). \tag{2}$$

3. The first residual is:

$$r_1(t) = x(t) - \overline{f}_1(t). \tag{3}$$

4. Through the obtained $r_1(t)$, the second IMF is derived from decomposing $r_1(t) + \varepsilon_1 E_1 \omega^i(t)$ again:

$$\overline{f_2}(t) = \frac{1}{N} \sum_{i=1}^{N} E_1 \left[r_1(t) + \varepsilon_1 E_1 \left(\omega^i(t) \right) \right]. \tag{4}$$

where $E_j(\cdot)$ is the $j = 2, 3 \dots J$-th IMF component.

5. Calculated from $j = 2, 3, \dots, J$, the j-th residual component is also available:

$$r_j(t) = r_{j-1}(t) - \overline{f}_j(t). \tag{5}$$

6. Calculated sequentially, the $j + 1$-th IMF component is as follows:

$$\overline{f}_{j+1}(t) = \frac{1}{N} \sum_{i=1}^{N} E_1 \left[r_j(t) + \varepsilon_j E_j \left(\omega^i(t) \right) \right]. \tag{6}$$

Repeat steps 5 and 6, if the residual component is a monotonic function, the decomposition is stopped:

$$r(t) = x(t) - \sum_{j=1}^{J} \overline{f}_j(t). \tag{7}$$

After the above steps, the signal after CEEMDAN can be expressed as

$$x(t) = \sum_{j=1}^{J} \overline{f}_j(t) + r(t). \tag{8}$$

3.2 Wavelet threshold

Wavelet coefficients gained from the decomposition of the soft threshold function have good continuity and do not oscillate. The resulting signal is also smooth, so the soft threshold is used in this paper. It can be expressed as:

$$\overline{\omega} = \begin{cases} \text{sgn}(\omega_{j,k})(|\omega_{j,k}| - \lambda) & |\omega_{j,k}| \geq \lambda \\ 0 & |\omega_{j,k}| < \lambda \end{cases}. \tag{9}$$

where λ is the threshold, $\omega_{j,k}$ is the wavelet coefficient, sgn($\cdot$) is the sign function and $\overline{\omega}$ is the transformed wavelet coefficient.

3.3 Autocorrelation normalization function

Figure 4 shows the features of the autocorrelation normalization function for the ordinary and noise signals. Both signals reach a peak at zero points, but the value of the noise signal tends to zero independently of time, while the value for normal signal fluctuates with time at other locations.
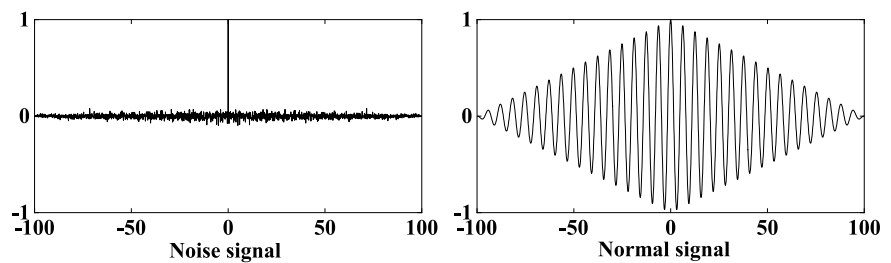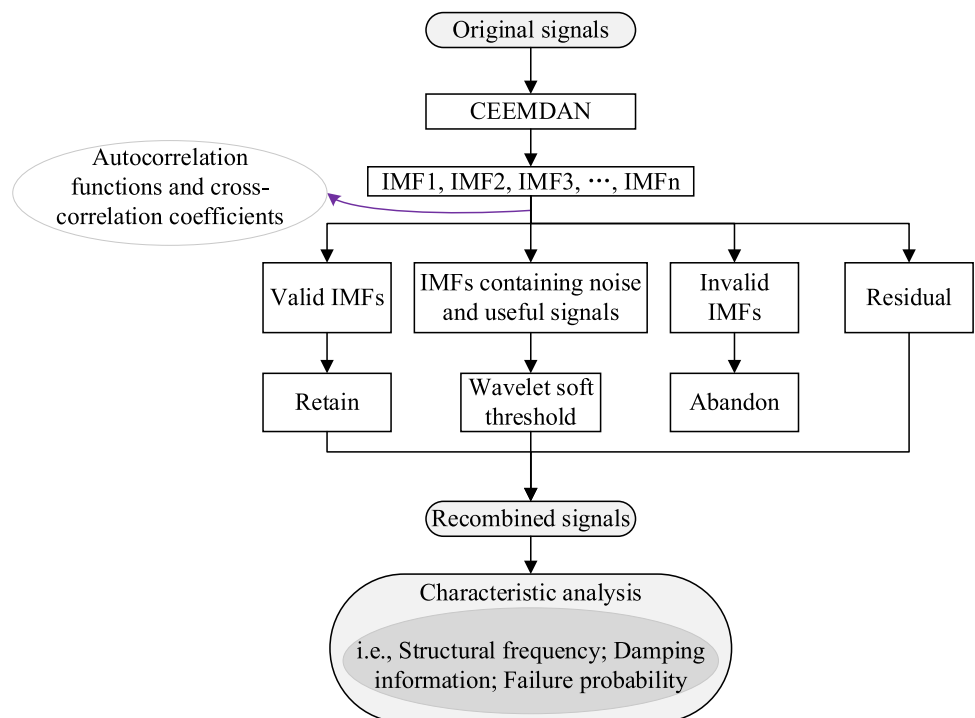
3.4 Cross-correlation coefficient

$$R = \frac{\sum_{t=0}^{\infty} x(t)\overline{f}_i(t)}{\sqrt{\sum_{t=0}^{\infty} x^2(t) \sum_{t=0}^{\infty} \overline{f}_i^2(t)}}, \tag{10}$$

where $\overline{f}_i(t)$ is each IMF, and R ($|R| \leq 1$) is the cross-correlation coefficient; the larger the value of R, the better the correlation of each IMF with the original signal. Here, R is one of the indicators and combines with the autocorrelation function to choose key IMFs.

3.5 Experiment processes

The experimental procedure in Fig. 5 involves two parts. In the first part, (a) the dynamic monitoring results of the super-high-rise building and the long-span bridge are used as the original signals. (b) CEEMDAN is performed to get a series of IMFs, and two methods of R and the autocorrelation function are combined to screen IMFs. Valid IMFs are

Fig. 4 Autocorrelation normalization function of different signals

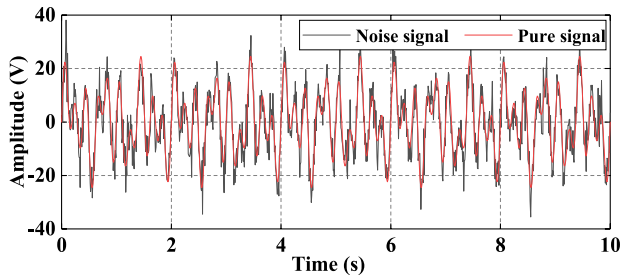**Fig. 5** The experimental flowchart

Fig. 6 Analog signal

reserved, noisy IMFs with low or no signal are discarded. (c) Wavelet soft thresholds are conducted on IMFs that contain both useful information and noise. Finally, the IMFs without processing are recombined with noise-reduced IMFs and corresponding residual components to get a reconstructed signal. In the second part, the dynamic characteristics of the two structures are extracted based on the reconstituted signal. It is worth noting that the accelerometer and RTK-GNSS monitor the main span together during the test on the bridge.

4 Engineering monitoring by RTK-GNSS

4.1 Performance evaluation of CEEMDAN

Before the actual experiment, a simulation test for CEEMDAN was done to verify its reliability and identify the advantage in reconfiguration:

$$
\begin{cases}
x_1(t) = A_1 \sin(2\pi \times 1.5t) \\
x_2(t) = A_2 \sin(2\pi \times 3t) \\
x_3(t) = A_3 \sin(2\pi \times 5t) \\
x(t) = x_1(t) + x_2(t) + x_3(t) \\
X(t) = x(t) + n(t)
\end{cases}
\tag{11}
$$

Taking Eq. (11) as an example, where $A_1 = 7$, $A_1 = 9$, $A_1 = 11$, $X(t)$ is composed of three sine signals and a random noise signal $n(t)$, where $x(t)$ represents the pure signal, as shown in Fig. 6.

In Fig. 6, because of noise, the actual value of the original pure signal cannot be accurately identified. Then the signal was recombined with EEMD and CEEMDAN, respectively.

In Fig. 7, the maximum absolute value of the recombination error of EEMD is 0.48, while CEEMDAN has a minor error (5×10^{-15}); the RMS results of both are 0.0125 and 1.837×10^{-15}. From Fig. 8, the signal after noise mitigation by CEEMDAN matches better with the original pure signal than EEMD. More importantly, CEEMDAN can also improve computational efficiency and save computing time.
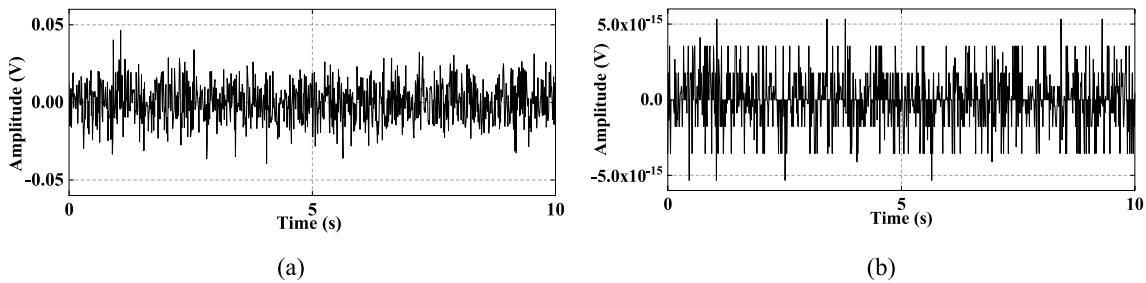

(a)

(b)

Fig. 7 Reconstruction errors: **a** EEMD; **b** CEEMDAN
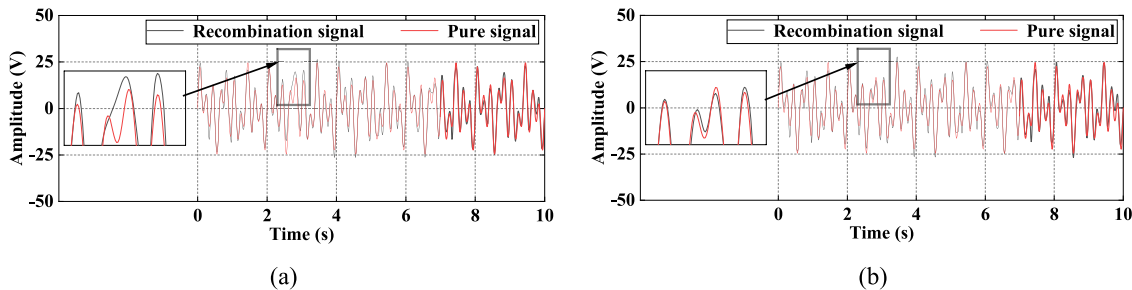

(a)

(b)

Fig. 8 Comparison between the reconstructed signal and the pure signal: **a** the pure signal and the signal reconstructed by EEMD; **b** the pure signal and the signal reconstructed by CEEMDAN

Fig. 9 The super-high-rise building

4.2 Dynamic monitoring of the super-high-rise building

4.2.1 Introduction for the object

The Tianjin Radio and television tower (Tianta) in Fig. 9 is a super-high-rise building. Tianta, which stands at the height of 415.2 m, was built in 1991 primarily for tourism, entertainment, and TV broadcasting. It is now the sixth-tallest tower in Asia and the third tallest in China. Moreover, it is the only tower located in a water environment in the world.

Tianta is a reinforced concrete tube-in-tube structure that consists of a tower base, tower body, tower, antenna, and other components. The inner tube contains an elevator and fire ladder. The outer barrel is cylindrical, with a diameter gradually decreasing from 36.5 m at the bottom to 12.5 m at the top. The incline changes every 10 m, and the wall thickness slowly decreases from 1.8 to 0.7 m. Tianta was built 30 years ago and exposed to long-term wind loads, lake water, and other factors that may lead to the aging and deformation of the structural elements.

4.2.2 Experimental implementation

The experiment was on January 13, 2021, in Tianjin of China. The humidity was 18%, the temperature was 9 °C, and the wind speed was 1.2–6.6 m/s. The main instruments were four RTK receivers that simultaneously received GPS, GLONASS, and BDS satellite signals. The receiving stations were 242–278 m of the Tianta tower, considering structure, instrument installation location, and local environment. Three RTK receivers were regarded as mobile stations (D1, D2, D3) in the east, west, and south at the height of 274 m. The north direction is obscured, so there was no monitoring point. The other receiver acted as a reference station on the open ground 100 m from the mobile station, as shown in Fig. 10. The sampling frequency was enhanced from 1 to 10 Hz with a height cut-off angle of 15°. The experiment continued for 10 h.

4.2.3 Hybrid filter noise reduction and results analysis

Table 2 gives the horizontal displacement changes of the above three monitoring points. The drift ratio (the ratio of the horizontal displacement to the measured height) is from 0.007 to 0.03%. The displacement change of D3 in the north–south direction is larger than that in the east–west direction, while D1 and D2 are opposite. The maximum displacement of D1 in the east–west reaches 97.1847 mm, primarily because of the wind direction and speed.

Fig. 10 The mobile stations and reference station: **a** in the south; **b** in the east; **c** in the west **d**; the reference station
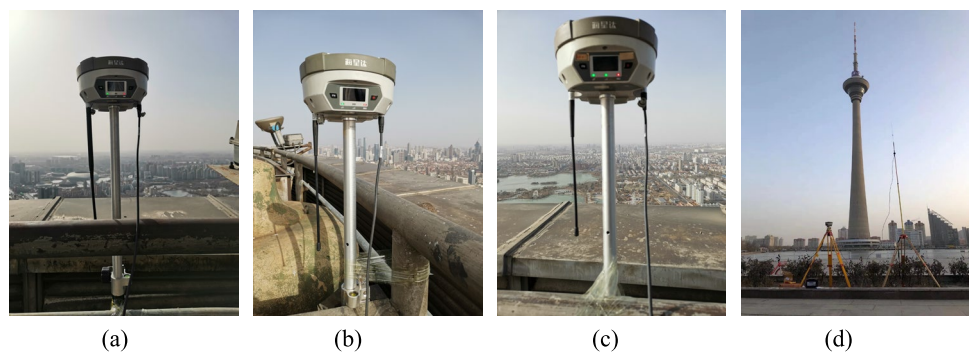

| (a) | (b) | (c) | (d) |

Table 2 Horizontal displacements of three monitoring points

	D1	D2	D3
North–South (mm)	− 30.6244 to 28.8285	− 20.5179 to 29.5902	− 38.1344 to 37.4552
East–West (mm)	− 53.1727 to 97.1847	− 47.3092 to 38.4979	− 29.0875 to 35.6217

Partial data of D3 were selected for analysis. The displacement in Fig. 11 changed within ± 40 mm, and the values in the north–south direction (F) were overall larger than those in the east–west direction (V), consisting with the trend of D3 in Table 2. Since the distance between the reference station and the mobile station is limited to 100 m, and it is known from Sect. 2 that the background noise dominated by multipath is the significant error source, it overwhelms the monitoring information.

CEEMDAN was conducted on the signals (F, V) and the results are shown in Fig. 12a, b. Signals were decomposed into 14 IMF with one residual component; each IMF reflected its local information characteristic. The high-frequency IMFs contained many noise components but could not be accurately identified. Figure 12c, d show the characteristics of the autocorrelation normalization for each IMF, and according to the definition in Sect. 3.3, the first eight IMFs are primarily noisy. If discarding those IMFs directly, the useful information could not be retained to the greatest extent. Therefore, the cross-correlation coefficient was used to further select IMFs.

In Table 3, the R values of IMF1–IMF6 in F and IMF1–IMF5 in V are comparatively small as invalid IMFs, while the remaining IMFs complete the first reorganization of the signal. Then, the db6 wavelet soft threshold is applied to IMF7–IMF8 in F and IMF6–IMF8 in V. The denoised IMFs are recombined with the unprocessed IMFs and residuals to accomplish the second recombined signal.

Figures 13 and 14 show that the displacement (F_1, V_1) changed within ± 30 mm, and the structure underwent a short-period motion without long-term irreversible deformation. Tianta could be treated as a variable-section cantilever structure. Its motion under the horizontal thrust dominated by wind load presented a reversible alternating vibration
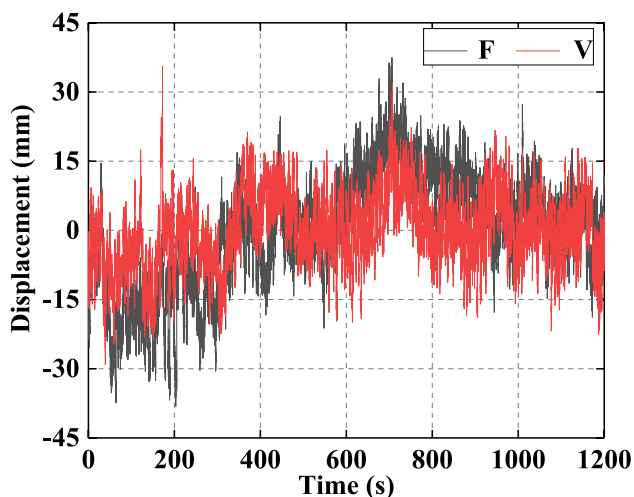
response consistent with the structure's planar motion, and the real-time displacement could be observed relatively clearly. Simultaneously, the other three methods are run to illustrate the proposed method's reliability. The evaluation criteria were the signal-to-noise ratio (SNR), root mean square error (RMSE), and R. The RMSE value decreased and the SNR increased, indicating that the better the denoise effect, the smaller the fitting error between the noise-reduced signal and the original signal.

Table 4 shows that EEMD had the poorest noise reduction, with the smallest SNR and the largest RMSE values; CEEMDAN is better than EEMD, but not significantly. In V_1, the SNR value of EEMD-Chebyshev is greater than that of EEMD, yet the fitness and correlation with the original signal are poor due to excessive noise reduction. However, CEEMDAN-WT mixed filtering has the highest SNR values (10.496 dB, 7.482 dB) and the lowest RMSE values (3.570 mm, 3.096 mm). Besides, after the proposed noise reduction method, the R values of the reconstructed signal and the original signal are 0.959 and 0.923, which are also higher than the other three methods. The above analysis indicates that the proposed technique achieves adequate noise reduction and retains useful information well, proving its superiority.

Figure 15 shows the corresponding power spectrum densities (PSDs) of F_1 and V_1, and the first-order frequency is 0.1583 Hz. The second and third-order frequencies are in a narrow frequency band. Based on the structural frequency and sampling frequency (10 Hz), the vibration period calculated is about 6.32 s, so the samples for two vibration cycles (120 data points) were selected randomly from the signal before and after noise reduction. Then, every 10 data points were averaged to get 12 sampling points, the motion trajectory (Fig. 16) in the plane direction was fitted based on the least squares method. Finally, the primary vibration direction of the structure in terms of the trajectory tilt angle iteratively calculated is about 35°37' from north to east.

In 2014, our team tested Tianta and established the FEM to pick up the modal frequencies (0.1586, 0.2250, 0.2763, 0.3785, 0.4581 Hz) [43]. In the previous experiment, the instrument sampling frequency was 1 Hz, and there was some occlusion at the placement, so only the first-order frequency (0.1590 Hz) was gained, and the error with the FEM was 0.252% [43]. This time, by enhancing the sampling rate and proposing a mixed noise reduction method, the first three modal frequencies in dense mode are obtained. The error between the first-order frequency and the FEM is 0.189%, smaller than the prior error. In Table 5, the errors of the third-order frequencies with FEM are relatively small, 4.379% and 2.895%, respectively. This experiment extracted the first three modal frequencies of the low-frequency structural response perfectly, and Tianta maintains stability

Fig. 11 Original displacement

Fig. 12 CEEMDAN decomposition and autocorrelation normalization function: **a** IMFs derived from F; **b** IMFs derived from V; **c** autocorrelation function of IMFs for F; **d** autocorrelation function of IMFs for V
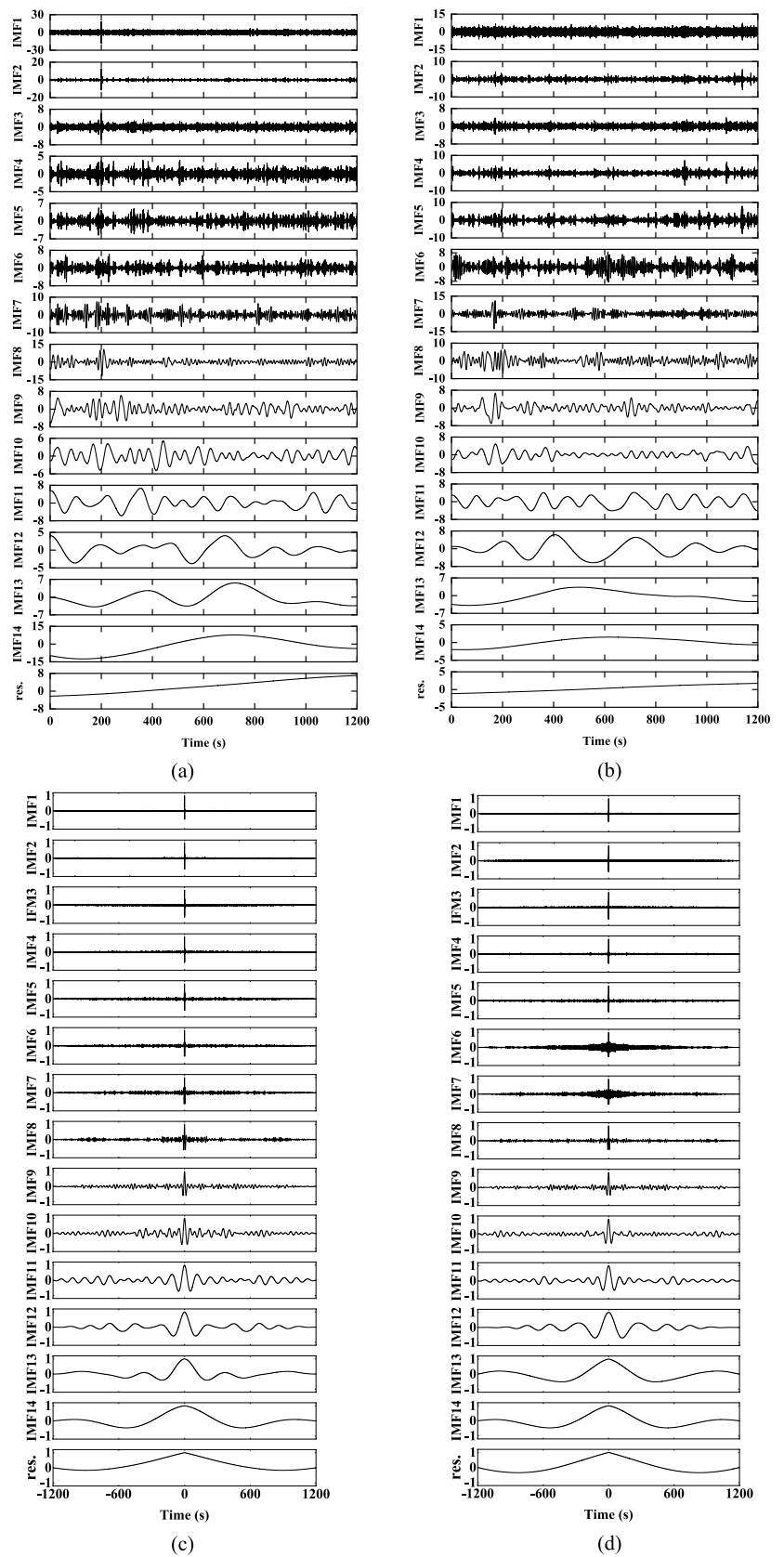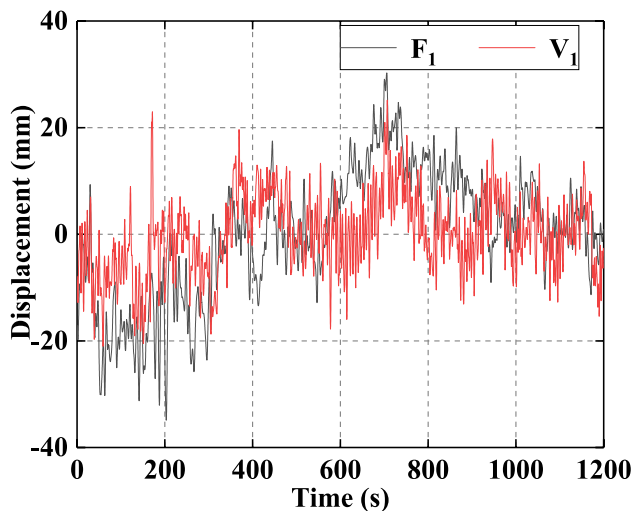
Table 3 Cross-correlation coefficients of the analyzed signal and each IMF

IMFs	Coefficient		IMFs	Coefficients	
	F	V		F	V
IMF1	0.175	0.249	IMF9	0.247	0.312
IMF2	0.103	0.145	IMF10	0.221	0.343
IMF3	0.109	0.157	IMF11	0.248	0.391
IMF4	0.119	0.204	IMF12	0.301	0.397
IMF5	0.146	0.263	IMF13	0.534	0.362
IMF6	0.181	0.411	IMF14	0.702	0.390
IMF7	0.216	0.351	Res	0.563	0.323
IMF8	0.238	0.340			

Fig. 13 Displacement after noise reduction
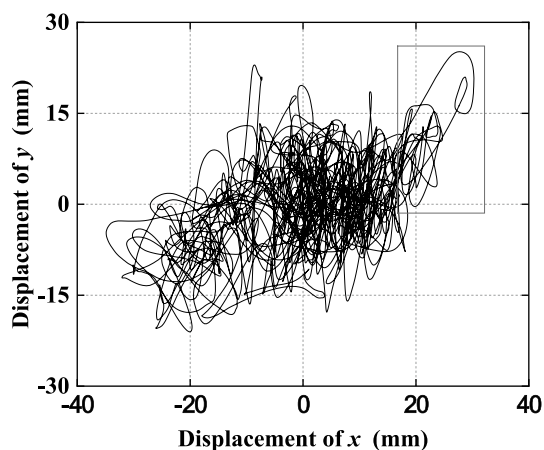
Fig. 14 Planar displacement

without significant changes in intrinsic frequencies over a long period.

4.3 Dynamic characteristic analysis of the suspension bridge

4.3.1 Description of the Fumin bridge

Fumin bridge is an important traffic hub between the Hedong and Hexi Districts of Tianjin in China. It runs north to south and officially opened to traffic in 2008. Figure 17 is the overall view. Its structural type is a concrete self-anchored suspension bridge with a total span of 340.3 m (Fig. 18). The bridge is 38.6 m wide with six two-way lanes; a guardrail protects the lanes and sidewalks. The main span is 157 m. The bridge tower is a single 58 m tower, and the side span is anchored by a set of cables (two side by side, without vertical slings). The principal span is fixed on both sides with 14 plus vertical slings for cables. According to the traffic statistics for the bridge, an average of 25 vehicles per minute pass, primarily small cars, and the bridge vibration is noticeable when large trucks pass. The bridge is located in a prosperous area of Tianjin and is exposed to a corrosive water environment.

4.3.2 Instrument arrangement

The instrumentation consisted of two triaxial accelerometers, one velocimeter, and seven RTKs, one of which served as a reference station, with the remaining six as mobile stations. They were placed symmetrically at the side span (M1) and the main span (M2 and M3). Accelerometers were also symmetrically arranged on M2 (Figs. 18 and 19). The east–west, north–south, and vertical directions along the bridge are x, y, and z.

Mobile stations were fixed by a support rod instead of a tripod to prevent the displacement by bridge deck vibration. Meanwhile, the horizontal bubble on its surface ensures that the support rod is vertical. The reference station was installed on open ground, and the distance was 100 m, 150 m, and 200 m from M1, M2, and M3, respectively. In addition, the axis of the accelerometer was aligned with the center of the RTK to ensure that they were at the same point.

The experiment lasting 10 h was on September 17th, 2020. The winding temperature was 21–26.8 °C, the wind speed was 2.1–6.2 m/s. During the experiment, there were more than ten satellites available, and the horizontal dilution of precision (HDOP) was 0.8–1.1. The altitude cut-off angle was 15°, the RTK and accelerometer sampling rates were 10 and 100 Hz.

4.3.3 Data processing and characteristic analysis

The bridge exhibits a stochastic vibration when subjected to random dynamic loads. The vehicle load had a more significant impact on the vertical vibration than the wind, so

Table 4 Noise reduction results by different methods

Signals	Criterion	EEMD	CEEMDAN	EEMD-Chebyshev	Proposed method
F_1	SNR (dB)	3.869	7.212	7.963	10.496
V_1		2.716	4.338	3.061	7.482
F_1	RMSE (mm)	5.717	4.991	5.010	3.570
V_1		4.439	4.077	5.647	3.096
F_1	R	0.911	0.917	0.916	0.959
V_1		0.838	0.862	0.752	0.923

Fig. 15 Power spectral density functions: **a** PSD of F_1; **b** PSD of V_1
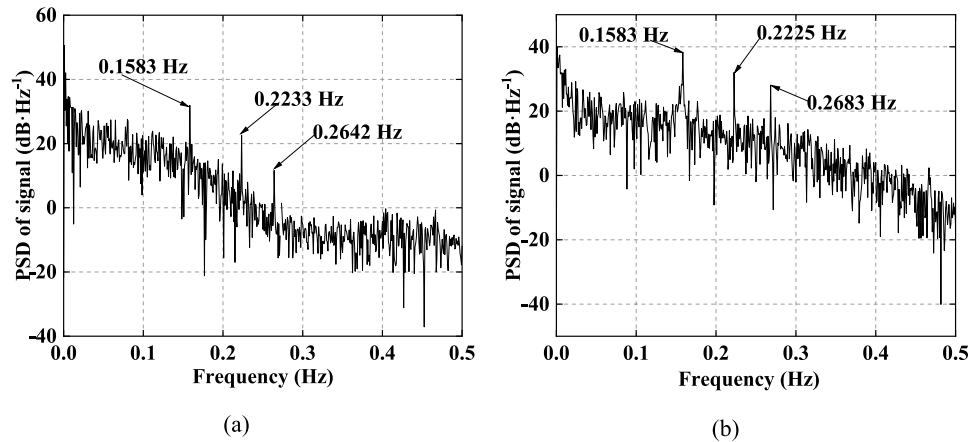
Fig. 16 Movement trajectory: **a** before noise reduction; **b** after noise reduction
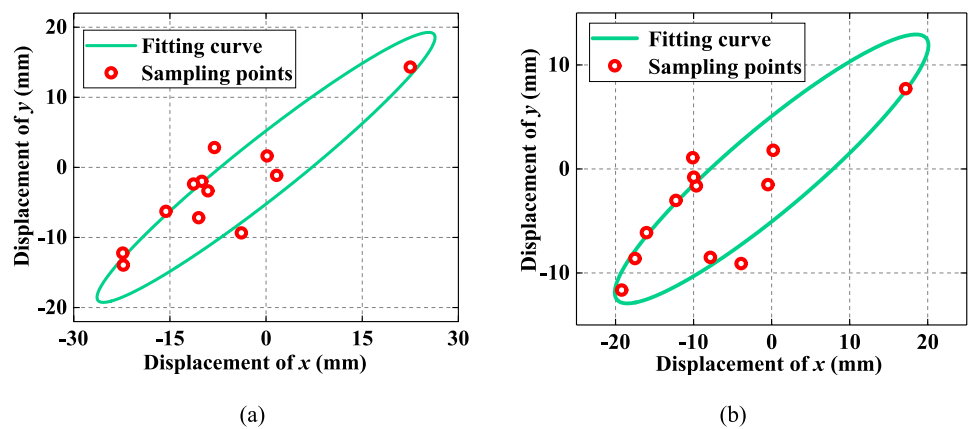
Table 5 Frequency errors

Orders	Frequency (Hz)			Errors (%)	
	F_1 signal (F_{f1})	V_1 signal (F_{v1})	FEM (F_{a1})	$\varepsilon_1 = \left\| \frac{F_a - F_{f1}}{F_a} \right\| \times 100$	$\varepsilon_2 = \left\| \frac{F_a - F_{v1}}{F_a} \right\| \times 100$
First	0.1583	0.1583	0.1586	0.189	0.189
Second	0.2233	0.2225	0.2250	0.756	1.111
Third	0.2642	0.2683	0.2763	4.379	2.895

recording the traffic load for 3 consecutive days at different periods. After multivariate analysis and classification, the numbers of vehicles of the same type passing through the bridge deck between 13:00 to 14:00 and from 16:30 to 17:30 were 17 and 56 vehicles per minute; thus, the partial
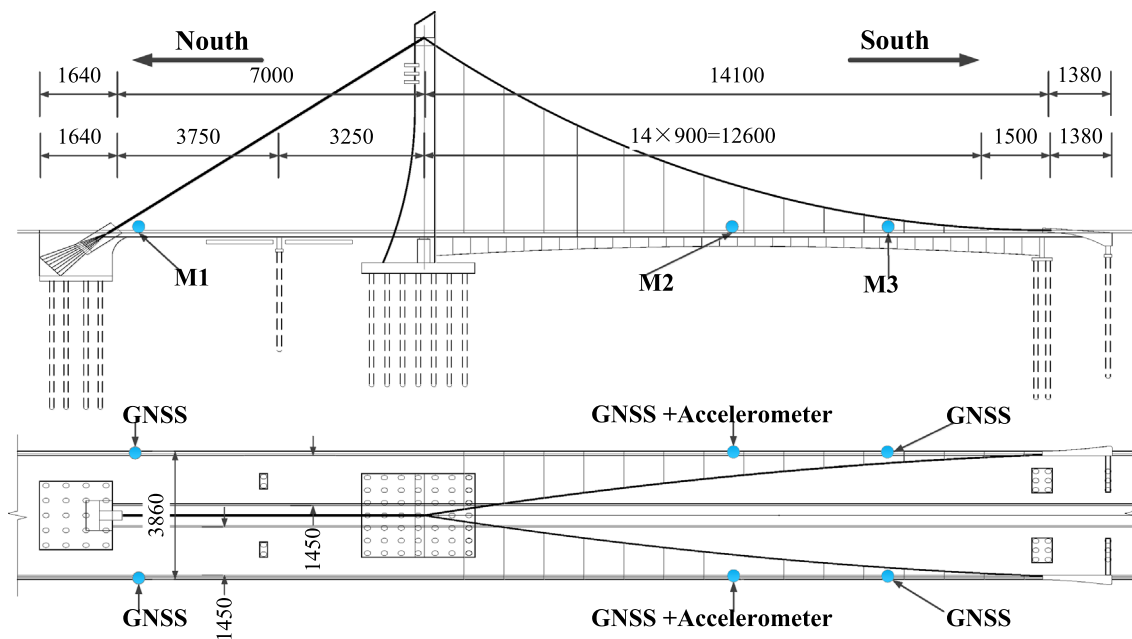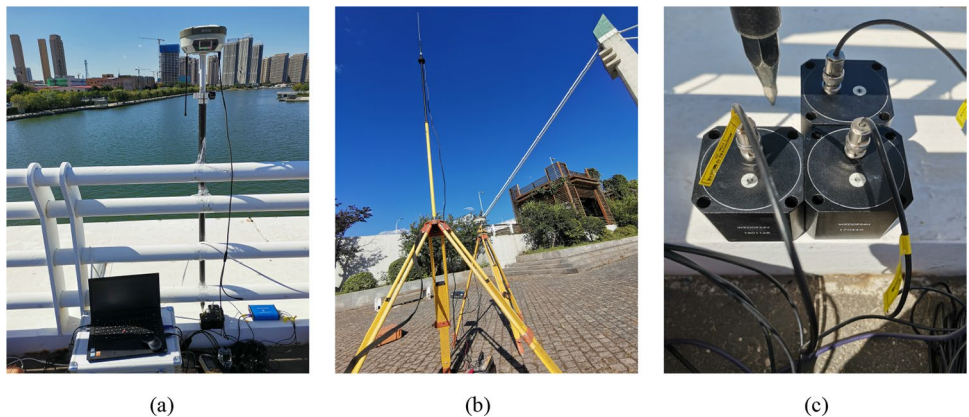
Fig. 17 Full view of Fumin bridge

Fig. 18 Schematic diagram of the bridge structure and sensor placement (unit: cm)

Fig. 19 Equipment layout: **a** the mobile station; **b** the reference station; **c** accelerometer

(a)   (b)   (c)

vertical displacement data (Z and H) from two time periods were selected.

In Fig. 20a, the displacements of Z and H were − 34.7 to 30.5 mm, − 47.7 to 43.3 mm, and the vertical deformation of H was higher, suggesting that more vehicles passed through in this period. The distance between the mobile station and the reference station was shorter than 300 m. The water area was closer to the bridge deck, exacerbating the effect of background noise.

The abnormal data were processed by the Pauta (3σ) criterion, then they were smoothed by a five-point cubic algorithm to procure Z_1 and H_1, as shown in Fig. 20b. Although noise pollution is slightly less than in Fig. 20a, it is still insufficient to identify displacement changes, necessitating reliable noise reduction further.

The hybrid filtering method in Sect. 4.2.3 was applied to get Z_2 and H_2. It can be seen from Fig. 21 that the noise interference was significantly relieved without altering the signal waveform. The corresponding R values of Z_2 and Z, H_2 and H were 0.938 and 0.961, respectively, showing that the correlation before and after the signal noise reduction was acceptable and retained valuable components. Figure 22a gives the PSDs of the residuals (G, W) after subtracting signals before and after noise reduction. We see no pronounced frequency peaks in the graph, meaning preserving the inherent frequency of the bridge while attenuating the noise. The PSDs of Z_2 and H_2 are shown in Fig. 22b. The first-order frequencies of the two signals are 0.761 Hz and 0.702 Hz. The inherent frequency of the bridge changed under the excitation of different traffic loads, but the change was small.

The RDT [44, 45] allowed obtaining the free decay responses of modes involving the intrinsic frequency, and the interception time considered was 30 s (Fig. 23) based on the actual situation of signals. The intense fluctuations for displacements and the limitation of the sampling length
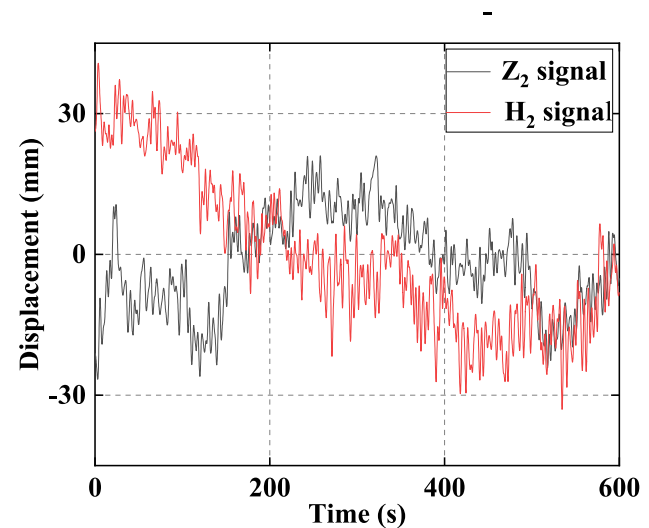

Fig. 21 Displacement after noise reduction (Z_2, H_2)

led to the random decrement signatures were not the most entirely ideal state but could be further treated as input responses to ITD [46]. After screening and eliminating the pseudo-modal values, the damping ratios extracted by ITD were 0.93% and 1.68%. The damping ratio rose with the increase of vehicles, thereby reflecting the dynamic working behavior of the bridge during operation.

4.3.4 Accelerometer results analysis

The monitoring results of the accelerometer and RTK were compared, choosing the part of the acceleration data in the same period as the Z for analysis. Figure 24 presents the results. Figure 25a showed that the first and second-order frequencies of the bridge were 0.774 Hz and 1.472 Hz, respectively. Comparing Figs. 22b and 25a, the first-order frequencies of Z_2, H_2, and C_2 were different. This indicated
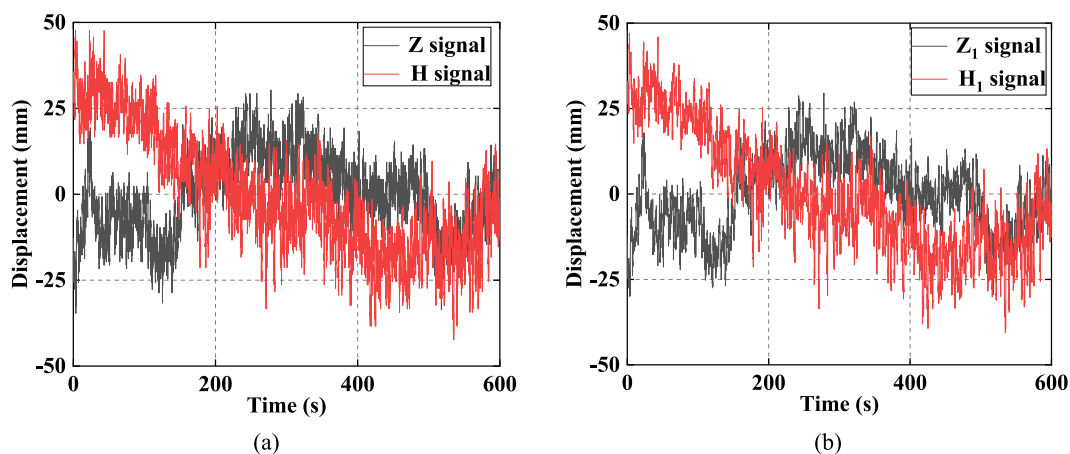

Fig. 20 Displacement: **a** original displacement (Z, H); **b** pre-processed displacement (Z_1, H_1)
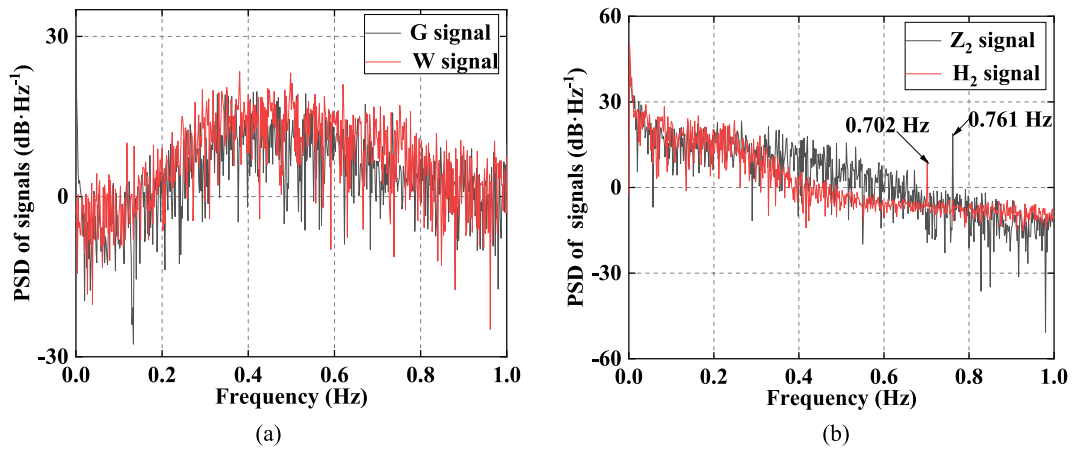
Fig. 22 The PSDs: **a** the PSDs of signal residuals (G, W); **b** the PSDs of Z_2 and H_2

Fig. 23 Free decay signatures: **a** free decay response of Z_2; **b** free decay response of H_2
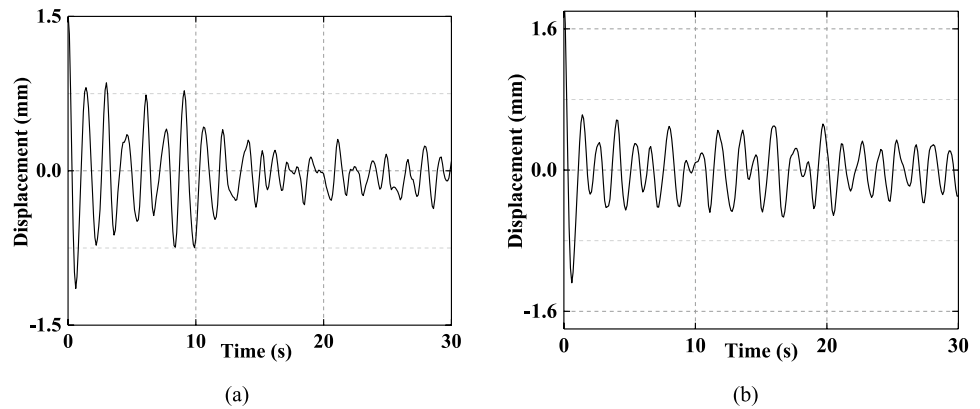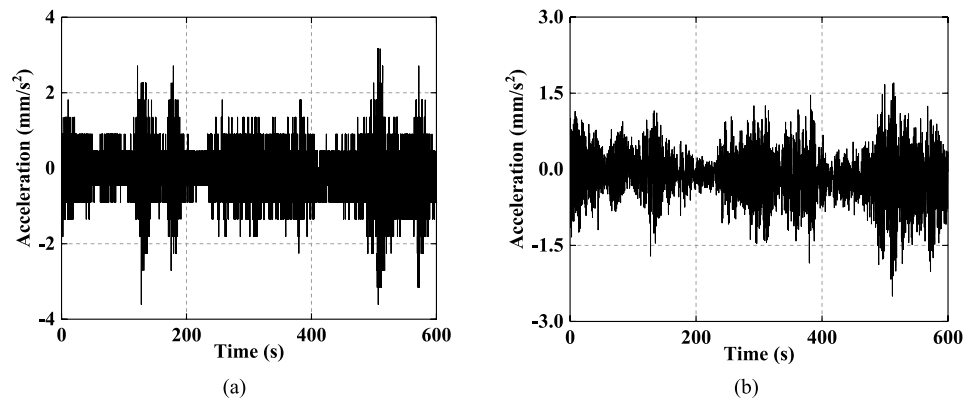

Fig. 24 Acceleration before and after noise reduction by hybrid filter: **a** original signal (C); **b** denoised signal (C_2)

that not only did the magnitude of the vehicle load change its frequency, but the frequencies obtained by different monitoring systems varied. Meanwhile, the accelerometer gained the second-order frequency. The 40 s data intercepted in signal C_2 was the response of RDT, and the first two order damping ratios identified by ITD were 2.77% and 0.39%.

4.3.5 Finite element verification

The ANSYS established a FEM (Fig. 26) of the bridge; each node had six degrees of freedom, i.e., translation and rotation of x, y, and z. Bridge decks, single towers, and longitudinal and transverse beams were adapted to BEAM44 element; the diagonal cables and upright booms applied the LINK10 element. The elastic modulus of the steel box

Fig. 25 The PSD function and free decay signature: **a** the PSD of C_2; **b** the free decay response of C_2
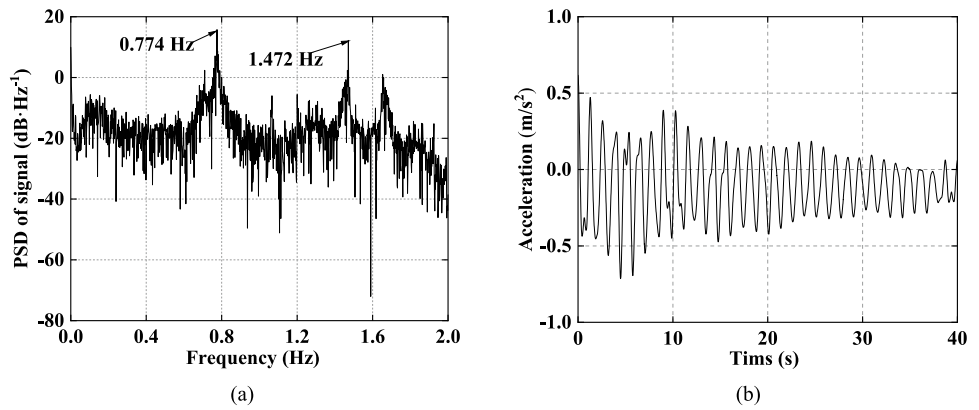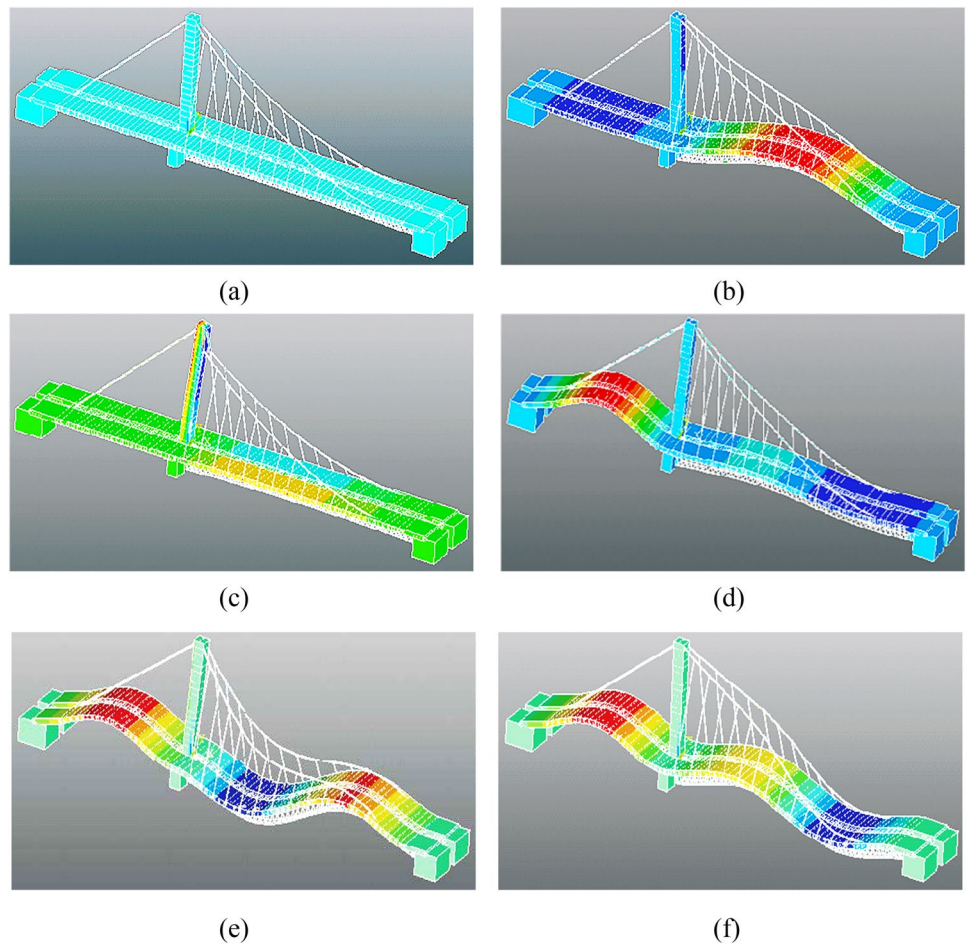

(a)

(b)

Fig. 26 The FEM and the first five modes: **a** the Fumin bridge model; **b** the first-order mode; **c** the second-order mode; **d** the third-order mode; **e** the fourth-order model; **f** the fifth-order mode

(a)

(b)

(c)

(d)

(e)

(f)

girder was 2.0×10^{11} Pa, the Poisson's ratio was 0.3. The analysis yielded the first five order frequencies of 0.743, 1.455, 2.491, 2.727, and 3.805 Hz. The third- and fourth-order frequency bands were narrower. Generally, the first three order frequencies were more meaningful for assessing structural performance.

The first-order frequency relative errors between the two sensors (Z_2 and H_2 derived from RTK-GNSS, C_2 obtained by accelerometer) and the FEM were 2.42%, 5.52%, and 4.17%; the second-order frequency relative error of C_2 with finite element was 1.17%. RTK could identify the first-order frequency and that the relative error procured by Z_2 was smaller than that of the accelerometer. The first-order frequency of H_2 had the largest relative error, more than 5%. However, the accelerometer could identify more frequencies, and the relative errors were within reasonable ranges.

When the height cut-off angle and sampling rate were all the same, RTK could identify the first three order frequencies from the horizontal displacement after noise reduction of Tianta, but only the first-order frequency from the denoised vertical displacement of the Fumin bridge. There are two reasons possibly for this. First, RTK-GNSS is more sensitive to low-frequency responses, and the horizontal positioning accuracy of RTK is better than that of vertical positioning. Second, the modal frequencies of the super-high-rise building will not change under short-time low-speed wind loads, while the effect of random vehicles results in a reduced contribution for higher order modes of the bridge and fails to detect more frequencies. A solution would be to continuously increase the sampling rate of RTK-GNSS to improve the monitoring accuracy and identify higher order frequencies of bridges.

4.3.6 Security assessment

The probability density function (PDF) illustrates the safety of a bridge more conveniently. According to the Specifications for Design of Highway Suspension Bridge of China (JTG/T D65-05–2015), the maximum allowable vertical displacement of the stiffened girder is 1/250 of its span. The maximum deflection calculated was ± 18 mm using the design standard section length (4.5 m). In general, bridge vibration signals conform to the Gaussian distribution, and the function is as follows:

$$P_f = 1 - P(a \le X \le b) = 1 - \int_a^b f(x)\mathrm{d}x, \tag{12}$$

where X is the displacement, $a = -18$ mm, $b = 18$ mm. Two key parameters need to be determined, namely the mean and standard deviation. The mean values for signals in Fig. 21 were -1.49 mm and -0.029 mm; the standard deviations were 10.59 mm and 16.39 mm. Figure 27 presents the PDF.

Depending on Eq. (12), the P_f values are 0.105 and 0.257, suggesting that the bridge had an increased probability for local structural failure in a short time under the impact of congested traffic. However, it is still within a safe range. Consequently, the PDF can be used to control the magnitude of daily bridge traffic volume and contribute a quantitative reference for achieving a regular structural reliability assessment.

5 Conclusions

This article investigated the dynamic deformation of two large civil structures via RTK-GNSS technology, demonstrating the practicality of the GNSS system for providing
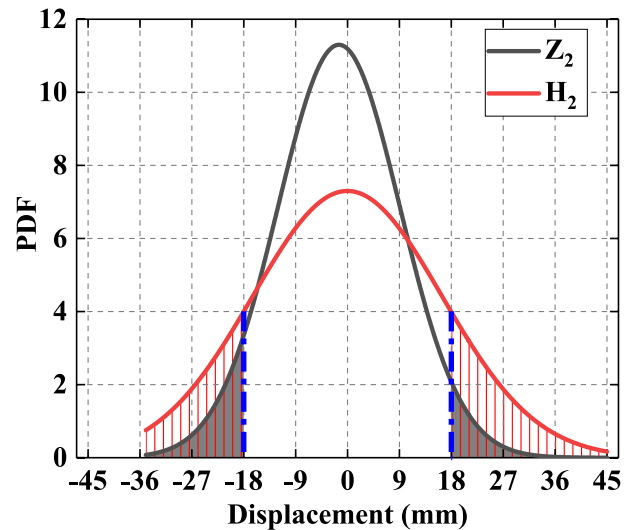

Fig. 27 The PDFs of Z_2 and H_2

structural modal parameters, real-time behavior characteristics, and reliability assessment. Here are the conclusions summarized.

(1) The study analyzed the adverse effects of the water environment on the monitoring results and developed a CEEMDAN-WT hybrid filtering to attenuate the background noise. Compared with the other three methods (EEMD, CEEMDAN, and EEMD-Chebyshev), the practicability of the proposed hybrid filtering in denoising and information retention was confirmed after analyzing the SNR, RMSE, and correlation of denoised signals in the super-high-rise building. The method was equally valid for the data noise reduction of the Fumin bridge.

(2) More modal frequencies of the super-high-rise building were captured by evaluating the spectral characteristics of horizontal signals after noise reduction. Furthermore, the inaccuracy for the first-order frequency was smaller than in the earlier experiment. The super-high-rise building still maintained normal status with the natural frequency had no significant change after long-term use.

(3) The intrinsic frequencies and damping ratios of the Fumin bridge were picked up under different loads; their frequency relative errors with the FEM were 2.42% and 5.52%, illustrating that traffic burthen could cause variation for dynamic characteristics. In comparison, the accelerometer identified the first two frequencies and damping ratios perfectly. In addition, with the dramatic growth of short-time vehicle loads, the failure probability of the bridge increased from 0.105 to 0.257.

Declarations

Conflicts of interest The authors declare that there is no conflict of interest.

References

1. Yi TH, Li HN, Gu M (2013) Wavelet based multi-step filtering method for bridge health monitoring using GPS and accelerometer. Smart Mater Struct 11(4):331–348. https://doi.org/10.12989/sss.2013.11.4.331

2. Kim K, Choi J, Chung J, Koo G, Bae IH, Sohn H (2018) Structural displacement estimation through multi-rate fusion of accelerometer and RTK-GPS displacement and velocity measurements. Measurement 130:223–235. https://doi.org/10.1016/j.measurement.2018.07.090

3. Yuan K, Zhu W (2021) Estimation of modal parameters of a beam under random excitation using a novel 3D continuously scanning laser Doppler vibrometer system and an extended demodulation method. Mech Syst Signal Proc 155:107606. https://doi.org/10.1016/j.ymssp.2021.107606

4. González-Aguilera D, Gómez-Lahoz J, Sánchez J (2008) A new approach for structural monitoring of large dams with a three-dimensional laser scanner. Sensors 8(9):5866–5883. https://doi.org/10.3390/s8095866

5. Weisbecker H, Cazzolato B, Wildy S, Marburg S, Codrington J, Kotousov A (2012) Surface strain measurements using a 3D scanning laser vibrometer. Exp Mech 52(7):805–815. https://doi.org/10.1007/s11340-011-9545-5

6. Schlögl M, Widhalm B, Avian M (2021) Comprehensive time-series analysis of bridge deformation using differential satellite radar interferometry based on Sentinel-1. ISPRS-J Photogramm Remote Sens 172:132–146. https://doi.org/10.1016/j.isprsjprs.2020.12.001

7. Granello G, Andisheh K, Palermo A, Waldin J (2018) Microwave radar interferometry as a cost-efficient method of monitoring the structural health of bridges in New Zealand. Struct Eng Int 28(4):518–525. https://doi.org/10.1080/10168664.2018.1461538

8. Zhang G, Guo G, Li L, Yu C (2018) Study on the dynamic properties of a suspended bridge using monocular digital photography to monitor the bridge dynamic deformation. J Civ Struct Health Monit 8(4):555–567. https://doi.org/10.1007/s13349-018-0293-4

9. Chen SE, Rice C, Boyle C, Hauser E (2011) Small-format aerial photography for highway-bridge monitoring. J Perform Constr Facil 25(2):105–112. https://doi.org/10.1061/(ASCE)CF.1943-5509.0000145

10. Yu J, Meng X, Yan B, Xu B, Fan Q, Xie Y (2020) Global Navigation Satellite System-based positioning technology for structural health monitoring: a review. Struct Control Health Monit 27(1):e2467. https://doi.org/10.1002/stc.2467

11. Shen N, Chen L, Liu J, Wang L, Tao T, Wu D, Chen R (2019) A review of global navigation satellite system (GNSS)-based dynamic monitoring technologies for structural health monitoring. Remote Sens 11(9):1001. https://doi.org/10.3390/rs11091001

12. Li H, Nie G, Chen D, Wu S, Wang K (2019) Constrained MLAMBDA method for multi-GNSS structural health monitoring. Sensors 19(20):4462. https://doi.org/10.3390/s19204462

13. Ogundipe O, Lee JK, Roberts GW (2014) Wavelet de-noising of GNSS based bridge health monitoring data. J Appl Geod 8(4):273–282. https://doi.org/10.1515/jag-2014-0011

14. Wang X, Zhao Q, Xi R, Li C (2021) Li G (2021) Review of bridge structural health monitoring based on GNSS: from displacement monitoring to dynamic characteristic identification. IEEE Access 9:80043–80085. https://doi.org/10.1109/ACCESS.2021.3083749

15. Beshr AAA, Zarzoura FH (2021) Using artificial neural networks for GNSS observations analysis and displacement prediction of suspension highway bridge. Innov Infrastruct Solut 6(2):109. https://doi.org/10.1007/s41062-021-00458-4

16. Zhang R, Gao C, Pan S, Shang R (2020) Fusion of GNSS and speedometer based on VMD and its application in bridge deformation monitoring. Sensors 20(3):694. https://doi.org/10.3390/s20030694

17. Li X, Huang G, Zhang Q, Zhao Q (2018) A new GPS/BDS tropospheric delay resolution approach for monitoring deformation in super high-rise buildings. GPS Solut 22(3):1–12. https://doi.org/10.1007/s10291-018-0752-8

18. Xiong C, Niu Y (2019) Investigation of the dynamic behavior of a super high-rise structure using RTK-GNSS technique. KSCE J Civ Eng 23(2):654–665. https://doi.org/10.1007/s12205-018-0238-9

19. Roberts GW, Brown CJ, Tang X, Meng X, Ogundip O (2014) A tale of five bridges; the use of GNSS for monitoring the deflections of bridges. J Appl Geod 8(4):241–264. https://doi.org/10.1515/jag-2014-0013

20. Xin J, Zhou J, Yang SX, Li X, Wang Y (2018) Bridge structure deformation prediction based on GNSS data using Kalman-ARIMA-GARCH model. Sensors 18(1):298. https://doi.org/10.3390/s18010298

21. Yu S, Guo F, Zhang X, Liu W, Li X, Wu R (2018) A new method for GNSS multipath mitigation with an adaptive frequency domain filter. Sensors 18(8):2514. https://doi.org/10.3390/s18082514

22. Souza EM, Negri TT (2017) First prospects in a new approach for structure monitoring from GPS multipath effect and wavelet spectrum. Adv Space Res 59(10):2536–2547. https://doi.org/10.1016/j.asr.2017.02.043

23. Boccia L, Amendola G, Gao S, Chen CC (2014) Quantitative evaluation of multipath rejection capabilities of GNSS antennas. GPS Solut 18(2):199–208. https://doi.org/10.1007/s10291-013-0321-0

24. Niu Y, Ye Y, Zhao W, Shu J (2021) Dynamic monitoring and data analysis of a long-span arch bridge based on high-rate GNSS-RTK measurement combining CF-CEEMD method. J Civ Struct Health Monit 11(1):35–48. https://doi.org/10.1007/s13349-020-00436-x

25. Xu A, Wu J, Zhao R (2014) Wavelet-transform-based damping identification of a super-tall building under strong wind loads. Wind Struct 19(4):353–370. https://doi.org/10.12989/was.2014.19.4.353

26. Yi J, Zhang JW, Li QS (2013) Dynamic characteristics and wind-induced responses of a super-tall building during typhoons. J Wind Eng Ind Aerodyn 121:116–130. https://doi.org/10.1016/j.jweia.2013.08.006

27. He XH, Hua XG, Chen ZQ, Huang FL (2011) EMD-based random decrement technique for modal parameter identification of an existing railway bridge. Eng Struct 33(4):1348–1356. https://doi.org/10.1016/j.engstruct.2011.01.012

28. Wu Z, Huang NE (2009) Ensemble empirical mode decomposition: a noise-assisted data analysis method. Adv Adapt Data Anal 1(1):1–41. https://doi.org/10.1142/S1793536909000047

29. Yeh JR, Shieh JS, Huang NE (2010) Complementary ensemble empirical mode decomposition: A novel noise enhanced data analysis method. Adv Adapt Data Anal 2(2):135–156. https://doi.org/10.1142/S1793536910000422

30. Wu B, Gao Y, Ma N, Chanwimalueang T, Yuan X, Liu J (2021) Fault diagnosis of bearing vibration signals based on a reconstruction algorithm with multiple side Information and CEEMDAN method. J Vibroeng 23(1):127–139. https://doi.org/10.21595/jve.2020.21586

31. Fan Q, Meng X, Nguyen DT, Xie Y, Yu J (2020) Predicting displacement of bridge based on CEEMDAN-KELM model using GNSS monitoring data. J Appl Geod 14(3):253–261. https://doi.org/10.1515/jag-2019-0057

32. Mousavi AA, Zhang C, Masri SF, Gholipour G (2020) Structural damage localization and quantification based on a CEEMDAN Hilbert transform neural network approach: a model steel truss bridge case study. Sensors 20(5):1271. https://doi.org/10.3390/s20051271

33. Ye X, Sun Z, Chen B (2019) Research on modal parameters identification of bridge structure based on adaptive signal de-noising method. Cluster Comput 22(6):14377–14387. https://doi.org/10.1007/s10586-018-2301-1

34. Ni Y, Lu X, Lu W (2017) Operational modal analysis of a high-rise multi-function building with dampers by a Bayesian approach. Mech Syst Signal Proc 86:286–307. https://doi.org/10.1016/j.ymssp.2016.10.009

35. Naderpour H (2016) Fakharian P (2016) A synthesis of peak picking method and wavelet packet transform for structural modal identification. KSCE J Civ Eng 20(7):2859–2867. https://doi.org/10.1007/s12205-016-0523-4

36. Wu WH, Wang SW, Chen CC, Lai G (2019) Modal parameter identification for closely spaced modes of civil structures based on an upgraded stochastic subspace methodology. Struct Infrastruct Eng 15(3):296–313. https://doi.org/10.1080/15732479.2018.1547770

37. Kim S, Kim HK, Hwang YC (2018) Enhanced damping estimation for cable-stayed bridges based on operational monitoring data. Struct Eng Int 28(3):308–317. https://doi.org/10.1080/10168664.2018.1462132

38. Feng ZQ, Zhao B, Hua XG, Chen ZQ (2019) Enhanced EMD-RDT method for output-only ambient modal identification of structures. J Aerosp Eng 32(4):04019046. https://doi.org/10.1061/(ASCE)AS.1943-5525.0001034

39. Zhou W, Chelidze D (2008) Generalized eigenvalue decomposition in time domain modal parameter identification. J Vib Acoust-Trans ASME 130(1):011001. https://doi.org/10.1115/1.2775509

40. El Bouny L, Khalil M, Adib A (2019) ECG signal filtering based on CEEMDAN with hybrid interval thresholding and higher order statistics to select relevant modes. Multimed Tools Appl 78(10):13067–13089. https://doi.org/10.1007/s11042-018-6143-x

41. Ruiz-Aguilar JJ, Turias I, González-Enrique J, Urda D, Elizondo D (2021) A permutation entropy-based EMD–ANN forecasting ensemble approach for wind speed prediction. Neural Comput Appl 33(7):2369–2391. https://doi.org/10.1007/s00521-020-05141-w

42. Sun Z, Xi X, Yuan C, Hua YY (2020) Surface electromyography signal denoising via EEMD and improved wavelet thresholds. Math Biosci Eng 17(6):6945–6962. https://doi.org/10.3934/mbe.202035

43. Xiong CB, Niu YB, Li Z (2018) An investigation of the dynamic characteristics of super high-rise buildings using real-time kinematic–global navigation satellite system technology. Adv Struct Eng 21(5):783–792. https://doi.org/10.1177/1369433217732497

44. Hao W, Yang Q (2021) Applicability of random decrement technique in extracting aerodynamic damping of crosswind-excited tall buildings. J Build Eng 38:102248. https://doi.org/10.1016/j.jobe.2021.102248

45. Ku CJ, Cermak JE, Chou LS (2007) Random decrement based method for modal parameter identification of a dynamic system using acceleration responses. J Wind Eng Ind Aerodyn 95(6):389–410. https://doi.org/10.1016/j.jweia.2006.08.004

46. Siringoringo DM, Fujino Y (2008) System identification of suspension bridge from ambient vibration response. Eng Struct 30(2):462–477. https://doi.org/10.1016/j.engstruct.2007.03.004